

A coherence sweet spot with enhanced dipolar coupling

J. H. Ungerer,^{1, 2, 3,*} A. Pally,^{2, †} S. Bosco,⁴ A. Kononov,² D. Sarmah,² S. Lehmann,⁵ C. Thelander,⁵ V.F. Maisi,⁵ P. Scarlino,⁶ D. Loss,² A. Baumgartner,^{1, 2} and C. Schönenberger^{1, 2, ‡}

¹Swiss Nanoscience Institute, University of Basel, Klingelbergstrasse 82 CH-4056, Switzerland

²Department of Physics, University of Basel, Klingelbergstrasse 82 CH-4056, Switzerland

³Department of Physics, Harvard University, Cambridge, MA 02138, USA

⁴QuTech and Kavli Institute of Nanoscience, Delft University of Technology, Lorentzweg 1, 2628 CJ Delft, Netherlands

⁵Solid State Physics and NanoLund, Lund University, Box 118, S-22100 Lund, Sweden

⁶Institute of Physics and Center for Quantum Science and Engineering,

Ecole Polytechnique Fédérale de Lausanne, CH-1015 Lausanne, Switzerland

(Dated: May 20, 2024)

Qubits require a compromise between operation speed and coherence. Here, we demonstrate a compromise-free singlet-triplet (ST) qubit, where the qubit couples maximally to the driving field while simultaneously coupling minimally to the dominant noise sources. The qubit is implemented in a crystal-phase defined double-quantum dot in an InAs nanowire. Using a superconducting resonator, we measure the spin-orbit interaction (SOI) gap, the spin-photon coupling strength and the qubit decoherence rate as a function of the in-plane magnetic-field orientation. We demonstrate a spin qubit sweet spot maximizing the dipolar coupling and simultaneously minimizing the decoherence. Our theoretical description postulates phonons as the most likely dominant noise source. The compromise-free sweet spot originates from the SOI suggesting that it is not restricted to this material platform, but might find applications in any material with SOI. These findings pave the way for enhanced engineering of these nanomaterials for next-generation qubit technologies.

Qubits based on single localized spins in semiconductor nanostructures represent cutting-edge platforms for quantum information processing, boasting extended coherence times and benefiting from established industrial fabrication techniques [1]. Scaling-up electron spin qubits is challenging because of limitations in all-electrical control and their small electric and magnetic dipole moments. Complex structures such as microstrips or micromagnets are required to facilitate qubit manipulation [2, 3]. However, the inherent spin-orbit interaction (SOI) in confined semiconductor hole systems [4–8] and in electrons in nanowires (NWs) [9–13] offers an alternative coupling mechanism: SOI couples spin and charge degrees of freedom, enabling electric-dipole spin resonance [14–17] and spin-cavity coupling [9, 11, 13, 18–23].

SOI is particularly relevant in singlet-triplet qubits, where it introduces a hybridization gap, for example between the singlet $|S\rangle$ and spin-polarized triplet $|T^+\rangle$ states [24–26]. Recent experiments have demonstrated gigahertz-scale gaps, allowing to reach the strong coupling limit between these two-level systems and microwave resonators [22]. These experiments extended the list of systems with strong spin-photon coupling [21, 27–29] to even charge parity states.

Despite several reports of SOI induced material characteristics as a function of the magnetic field orientation [13, 21, 30–32], so far, only single sweet spots have been reported, either maximizing the coherence or the

operation speed as a function of a global tuning parameter. A recent report suggests that SOI could allow for simultaneous optimization of these two most relevant qubit parameters by local gates [33]. Here, we report that, in contrast to the common expectation, strong SOI allows one to simultaneously optimize both, the coherence and operation speed as a function of a global external parameter, here the angle of the applied magnetic field. We do so in a novel nanomaterial system with very reproducible characteristics.

We employ a magnetic-field resilient NbTiN resonator [34, 35] strongly coupled to a singlet-triplet ($S-T^+$) qubit in a crystal-phase defined InAs NW [22, 36, 37]. We apply an in-plane magnetic field in different orientations relative to the double quantum dot (DQD) [13, 21, 30, 38]. The coherent coupling between the resonator and the singlet-triplet qubit allows to measure the qubit transition frequency, the vacuum Rabi rate, and the qubit decoherence rate. Contrary to prevailing expectations, we identify a magnetic field orientation along the nanowire that serves as a compromise-free sweet spot, where a minimal decoherence rate coincides with a maximal dipolar coupling. These findings are well explained by a theoretical model that suggests phonons as dominant source of decoherence.

This non-trivial optimization of two conflicting qubit parameters with only one external parameter is inherent to systems with a strong SOI and demonstrates the remarkable potential of such semiconductor materials. Our results pave the way for future advances in material optimization and enhanced device functionality based on a deeper understanding of the underlying physics.

* Equal contributions.; jungerer@g.harvard.edu

† Equal contributions.

‡ nanoelectronics.unibas.ch

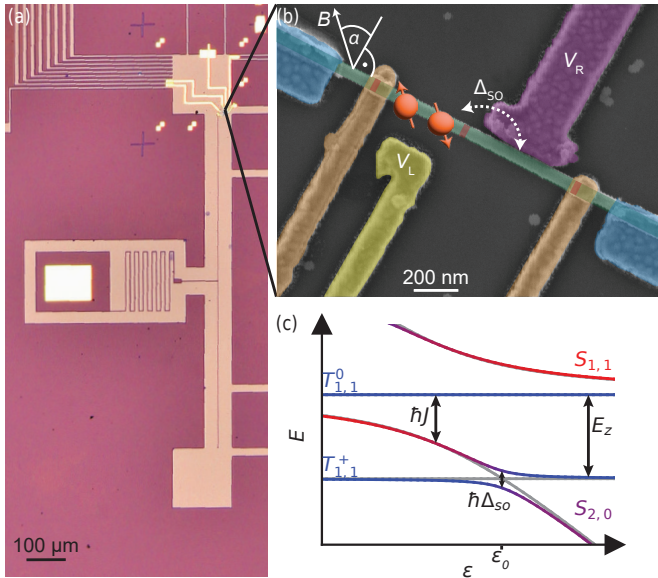


FIG. 1. **Superconducting resonator coupled to singlet-triplet qubit in a crystal-phase NW.** (a) Optical microscope image of the device showing a half-wave NbTiN resonator with a characteristic impedance of $2.1\text{ k}\Omega$. At the middle of the center conductor, a dc bias line is connected via a meandered inductor. (b) False-colored scanning electron micrograph of the crystal-phase NW device (image is rotated by -90° with respect to (a)). The NW is placed at the position indicated in (a) and the purple gate line is galvanically connected to the resonator at its voltage anti-node. Tunnel barriers (red) are indicated with arrows. The device is operated with an even electron filling as depicted schematically. During the experiments, the in-plane magnetic field angle α is varied using a vector magnet. (c) Level diagram for an even electron occupation as a function of the electrostatic detuning ε in the presence of strong SOI and finite magnetic field exhibiting singlet and triplet states. The avoided crossing between the spin-polarized triplet state T^+ and the low-energy singlet state at $\varepsilon = \varepsilon_0$ are detected using the resonator.

I. DEVICE

The device is depicted in Fig. 1. Detailed fabrication procedures are outlined in the Methods. This device comprises a superconducting half-wavelength coplanar-waveguide resonator coupled to a DQD formed by in-situ crystal-phase engineering in an InAs NW [22, 36, 37, 39].

Figure 1(a) shows an optical microscopy image of the resonator, fabricated by dry-etching an approximately 10 nm thick NbTiN film, atop a SiO_2 substrate [35]. The small thickness of the superconducting NbTiN renders the resonator resilient to in-plane magnetic fields [34, 35], and the narrow center conductor width, approximately 380 nm , combined with the large kinetic inductance of NbTiN, results in an impedance of $2.1\text{ k}\Omega$. This large impedance enhances the vacuum electric field fluctuation amplitude compared to standard $50\text{ }\Omega$ -type resonators, thereby increasing the dipolar coupling to the qubit [40].

The qubit is formed by electronic states in a DQD, with

tunnel barriers grown deterministically by controlling the InAs crystal phase during the vertical growth process of the NW [36, 37]. The barriers are highlighted in the the colored SEM image of Fig. 1(b) in red and indicated by arrows. The DQD forms within the zincblende segments of the NW, separated by wurtzite tunnel barriers. At finite magnetic fields and in an even electron configuration, the DQD states are singlet and triplet states, as depicted in the energy level diagram in Fig. 1(c). The ground state and first excited state comprise a superposition of the spin-polarized triplet $|T^+\rangle$, with an electron on each dot and the low-energy singlet state $|S_{2,0}\rangle$, with two excess electrons on one dot and none on the other. As depicted in Fig. 1(c), without spin-flip tunneling, the energy levels would cross at a detuning ε_0 at which the Zeeman energy E_z equals the exchange energy,

$$E_z = \hbar J \approx \frac{\hbar}{2} \left(\varepsilon_0 + \sqrt{\varepsilon_0^2 + 4t_c^2} \right), \quad (1)$$

where t_c is the inter-dot tunnel rate. But the finite inter-dot tunnel coupling and a substantial Rashba-type SOI in the zincblende segments [39] result in a spin rotation and in the hybridization of the original eigenstates, with an energy gap of $\hbar\Delta_{\text{so}}$ [24]. The two hybridized levels constitute a spin qubit with a spin orbit-mediated electric dipole moment that couples to the electric field fluctuations of the resonator, rendering the resonator an effective probe for quantitative measurements of the qubit parameters.

II. HYBRID SYSTEM AT LARGE MAGNETIC FIELDS

In our experiments, we measure the amplitude A and phase φ of a microwave probe tone transmitted through the resonator, capacitively coupled to the DQD. In Fig. 2(a), the squared normalized transmission amplitude $(A/A_0)^2$ through the resonator is plotted as a function of the probe frequency ω_p with the DQD tuned into Coulomb blockade, rendering it irrelevant for the measurement. This figure displays probe frequency scans at $|\mathbf{B}| = 0\text{ mT}$ and $|\mathbf{B}| = 100\text{ mT}$, where the field is applied in-plane. As visible in Fig. 2(a), the transmission though the resonator recorded for $|\mathbf{B}| = 0\text{ mT}$ and $|\mathbf{B}| = 100\text{ mT}$ does not show any variation, demonstrating that the resonator remains unaffected for the magnetic fields used in our experiments.

We now prepare the DQD in an even charge state [22, 41–43] and measure the resonator transmission at a frequency close to resonance. Figures 2(b), 2(c), 2(d), and 2(e) depict the transmission amplitude and phase as functions of the gate voltages V_L and V_R for in-plane fields of $|\mathbf{B}| = 0$ and $|\mathbf{B}| = 100\text{ mT}$.

Due to the electric-dipolar coupling between the resonator and the DQD, the resonator transmission directly reveals the charge stability diagram of the DQD [44]. At the inter-dot transition (IDT), the Zeeman energy and

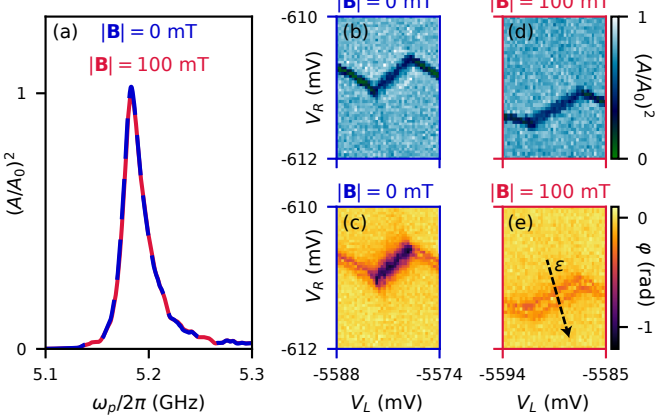


FIG. 2. Characterization of the hybrid device. (a) Resonator transmission $(A/A_0)^2$ as function of probe frequency ω_p . Fits to a lorenztian result in the resonance frequency $\omega_0/2\pi = 5.1854 \pm 0.0002$ GHz, and decay rate $\kappa/2\pi = 21.2 \pm 0.4$ MHz independent of the magnetic-field amplitude $|\mathbf{B}|$. The magnetic-field resilience of the resonator enables resonator-based investigation of the DQD. (b-e) Transmission $(A/A_0)^2$ and phase φ close to resonance frequency as a function of gate voltages V_L and V_R applied to the DQD as illustrated in Fig. 1(b) at zero field and at $|\mathbf{B}| = 100$ mT. Position and shape of the observed inter-dot transition signal varies as function of $|\mathbf{B}|$ due to an interaction of the resonator with spinful DQD levels.

the exchange energy are degenerate (see Eq. (1)) and the hybridized states form a qubit that couples to the resonator. The IDT can be easily identified, signaled by lines with positive slopes in Fig. 2(e).

Both, the position of the IDT in the gate-versus-gate map and the resonator response near the IDT strongly depend on the external magnetic field strength. This susceptibility to magnetic fields arises from the spin-dependent DQD transitions. In the following, we probe the resonator response as a function of electrostatic detuning ε which is manipulated by varying the gate voltages V_L and V_R along the line indicated in Fig. 2(e).

III. A DOUBLE SWEET SPOT

The main result of our work is represented by the dependence of the IDT characteristics on the in-plane field orientation. For this we show in Fig. 3(a) the resonator transmission phase φ close to the resonance frequency, plotted as a function of the in-plane angle α between the NW axis and the magnetic field, illustrated in Fig. 1(b) and Fig. 3(b), and versus the electrostatic DQD detuning ε as defined in Fig. 2(e). Fig. 3(a) reveals that the detuning ε_0 , at which the IDT is observed, varies as a function of α . This angle dependence can be understood qualitatively by recognizing that the SOI introduces an anisotropic g-tensor and hence determines the Zeeman energy E_Z and, according to Eq. 1, the position of the

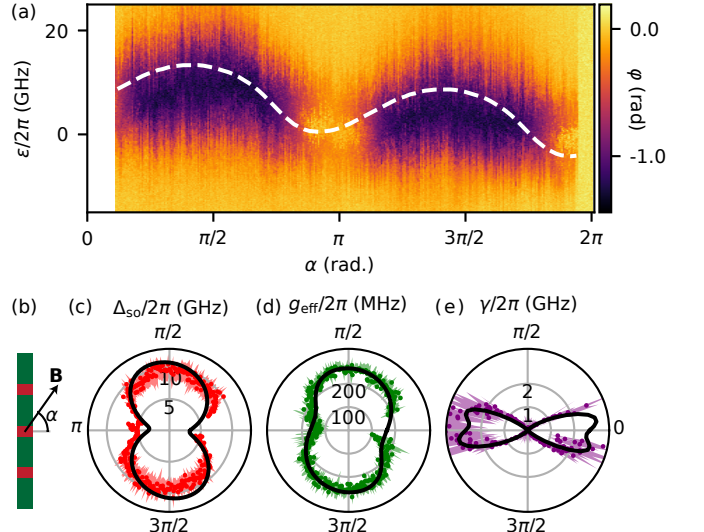


FIG. 3. Qubit parameters as function of in-plane field angle at $|\mathbf{B}| = 100$ mT. (a) Phase of the resonator transmission φ as function of electrostatic detuning ε and in-plane magnetic field angle α . The detuning ε , was calculated from the applied voltages, using the gate-to-dot lever arms (see Tab. I). The dashed curve corresponds to the position of the IDT in the theoretical model, $\varepsilon = \varepsilon_0$, to which a linear trend was added accounting for a drift of the gate voltage. (b) Schematic showing the alignment of the magnetic field \mathbf{B} with respect to the nanowire. (c) SOI gap Δ_{so} as function of α . (d) Qubit-resonator coupling strength g_{eff} as function of α . (e) Qubit decoherence rate γ as function of α . When the field is parallel to the NW, $\alpha = \pm\pi/2$, a compromise-free sweet spot is found where maximal qubit transition frequency and coupling strength coincide with minimal decoherence. (c), (d) and (e) are extracted using input-output theory. The streaks symbolize the uncertainty of the fit. This uncertainty is a consequence of the uncertainty of the gate lever arms which forms the most significant source of uncertainty in our experiment and is stated in the caption of Tab. I. All curves overlaid on the data result from the theoretical model described in the main text, using a single set of fit parameters.

IDT ε_0 . Furthermore, the phase signal as a function of ε changes continuously from a negative shift in φ at $\alpha \approx \pi/2$ [$3\pi/2$] to a double-dip structure at $\alpha \approx \pi$ [2π], because the SOI renders the magnitude of Δ_{SO} and the decoherence rate γ angle-dependent by affecting the overlap of the spin wavefunctions [24, 30, 38, 45]. For example, at $\alpha \approx \pi/2$, $\Delta_{\text{so}} > \omega_0$, resulting in a dispersive resonator signal. In contrast, at $\alpha \approx \pi$, $\Delta_{\text{so}} < \omega_0$ so that an (avoided) crossing between the singlet-triplet qubit and the resonator is observed as function of ε . This crossing experimentally results in a double dip structure in the $\varphi(\varepsilon)$ dependence, framing a positive shift at the center of the IDT, at $\varepsilon \approx \varepsilon_0$.

Using input-output theory [46] as described in the Methods, we extract the SOI gap Δ_{so} , the qubit decoherence rate γ , as well as the effective spin-photon coupling strength g_{eff} from the dependence of the resonator phase

and amplitude on ε . The results are plotted as function of in-plane angle α in Fig. 3(c), 3(d) and 3(e).

Excitingly, we find that, while Δ_{so} and g_{eff} are correlated with each other, they are anticorrelated with γ . In particular, when applying the magnetic field parallel to the NW, a compromise-free sweet spot is found, for which the spin-photon coupling strength g_{eff} is maximal while γ is minimal. To robustly estimate the spin-photon coupling and the decoherence rate at the sweet spot, we average over all extracted values in the interval $\alpha \in [55^\circ, 125^\circ] \cup [235^\circ, 305^\circ]$ and find $\langle g_{\text{eff}} \rangle / 2\pi = 250 \pm 15(30)$ MHz and $\langle \gamma \rangle / 2\pi = 11 \pm 20(400)$ MHz, where the error corresponds to the statistical (systematic) uncertainty. Here, the large systematic uncertainty originates from the uncertainty of the gate lever arms stated in the caption of Tab. I.

IV. THEORETICAL DESCRIPTION

In this section, we outline how the effective Hamiltonian yields the the dashed white and solid black curves shown in Figures 3(a), (c), and (d). The consecutive section describes how the decoherence is modeled (black curve in Fig. 3(e)).

All curves are the result of numerically diagonalizing the Hamiltonian H_5 in Eq. (12) in the Methods that describes the DQD states in proximity to the IDT. Thereby, we take into account an anisotropic g-tensor, identical for both dots, and a spin-orbit vector that is not aligned with the principal axes of the g-tensor. We point out that all curves are obtained from a single set of fit parameter, given in Table I. The Landé g-factor varies between $g = 10.5$ and $g = 5.25$, depending on the field direction. And, taking into account the distance of the two quantum dots, $d = 330$ nm, the spin-orbit length is found as $l_{\text{so}} = 130$ nm. These values are consistent with previous experiments [9, 47]. In Fig. 6 in the Methods, we use the fitted parameters to visualize the g-tensor.

After finding the eigenenergies and eigenstates from diagonalizing the Hamiltonian H_5 , we focus on the ground state $|0\rangle$ and first excited state $|1\rangle$ with their respective energies E_0 and E_1 . These form the qubit states which are sensed by the resonator. Because Eq. (1) is only valid for small SOI, which is not the case for certain field alignments, we more generally determine the detuning ε_0 , at which the anti-crossing occurs, by identifying the minimum gap for which

$$\partial_\varepsilon(E_1 - E_0) = 0. \quad (2)$$

The numerical solution for ε_0 is plotted in Fig. 3(a) on top of the data (white dashed curve). The variations of the detuning ε_0 of the IDT as function of α is caused by the g-tensor anisotropy. According to Eq. (1), this results in a variation of ε_0 at which the Zeeman energy equals the exchange energy. As a consequence, the detuning ε_0 at which the IDT is observed varies with the g-factor,

which in turn is given by the field orientation. Then, we numerically calculate the SOI gap

$$\Delta_{\text{so}} = E_1(\varepsilon_0) - E_0(\varepsilon_0), \quad (3)$$

plotted as solid black curve in Fig. 3(c). The variation of the SOI gap Δ_{so} is a consequence of the magnetic field orientation with respect to the anisotropic g-tensor and the spin-orbit vector. To calculate the vacuum Rabi coupling strength g_{eff} , we assume that the resonator couples to the electric dipole moment of the singlet-triplet qubit via the resonator vacuum fluctuations in the detuning of amplitude $\delta\varepsilon_0$ according to Eq. (11) in the Methods. This gives rise to the dipolar coupling strength as the vacuum Rabi rate

$$g_{\text{eff}} = \delta\varepsilon_0 |\langle 0 | h_{\delta\varepsilon} | 1 \rangle| \quad (4)$$

plotted as solid black curve in Fig. 3(d). Here, $h_{\delta\varepsilon}$ is the operator describing small variations of the detuning, given by Eq. (15) in the Methods and evaluated at the center of the IDT, $\varepsilon = \varepsilon_0$.

V. DECOHERENCE

In the experiment, using input-output theory, we utilize the resonator as a probe to extract the qubit decoherence rate γ , which is plotted in Fig. 3(e), and defined by

$$\gamma = \frac{\gamma_1}{2} + \gamma_\varphi, \quad (5)$$

where γ_1 is the relaxation rate and γ_φ the pure dephasing rate. The primary sources of decoherence in quantum dots are typically hyperfine-interaction induced dephasing from atomic nuclei [48–50], charge noise-induced dephasing [51–54], or relaxation due to phonons [55–63].

From our experiments, we extract an unexpected anti-correlation between the spin-photon coupling strength g_{eff} and the decoherence rate γ . Using our theoretical description, and Bloch-Redfield theory [56, 60, 64], we investigate various possible decoherence mechanisms as outlined in the Supplementary Material (SM). We find that consideration of magnetic noise stemming from nuclear spins or charge-noise due to phonons leads to the correct trend of γ as a function of the in-plane magnetic field angle α . However, because we identify decoherence rates comparable to the maximum of $\gamma(\alpha)$ also for a charge qubit at zero magnetic field, where magnetic noise is irrelevant, we hypothesize that phonons form the dominant noise source in our experiment. Therefore, here, we focus on phonon-mediated decoherence.

Fig. 3(e) and Fig. 4(a) show the phonon-mediated relaxation $\gamma_1^{\text{Ph}}(\alpha)$ as a function of the in-plane field angle α overlaid on the measured decoherence rate γ . Considering only the effect of a single gapless, low-energy phonon band gives rise to the analytical functional dependence $\gamma_1^{\text{Ph}}(\omega)$ as function of phonon frequency, ω (see

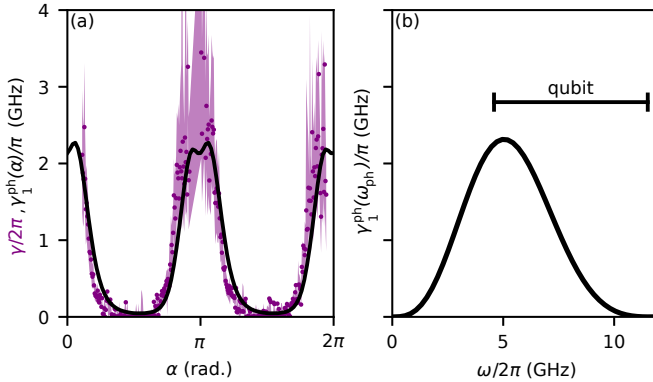


FIG. 4. **Phonons as possible decoherence source.** (a) Measured decoherence rate γ as a function of in-plane angle α (purple). The black curve is the numerically calculated relaxation rate $\gamma_1^{\text{ph}}(\alpha)$ originating from deformational phonons (see main text). (b) Analytical relaxation rate $\gamma_1^{\text{ph}}(\omega)$ as function of phonon frequency ω (see SM for details). The qubit operates in the frequency range as indicated with a negative slope of $\gamma_1^{\text{ph}}(\omega)$. This explains the anti-correlation between the SOI gap Δ_{so} and the decoherence rate γ - a possible reason for the compromise-free sweet spot formation.

SM for the derivation). This dependence is plotted in Fig. 4(b). These phonons lead to qubit relaxation when their frequency is close to the qubit transition frequency, $\omega \approx \Delta_{\text{so}}$. Because the phonon-mediated relaxation is maximal when the phonon wavelength is comparable to the size of the dots at $\omega \approx \omega_c$, an increase in Δ_{so} leads to a decrease in γ_1^{ph} . Therefore, a change in Δ_{so} as function of α results in the observed variations of γ_1^{ph} . In addition, variations of α result in a change of the electron-phonon coupling strength that enhances this effect and is considered in $\gamma_1^{\text{ph}}(\alpha)$, plotted as black curve on top of the data in Fig. 4(a).

In the SM, we discuss magnetic noise. Additionally, in the SM, we discuss $1/f$ -charge noise which does not capture the functional dependence of γ as a function of the in-plane magnetic field angle α .

VI. CONCLUSION

We have investigated a singlet-triplet ($S-T^+$) qubit strongly coupled to a magnetic-field resilient microwave resonator probing the qubit. We extract the SOI gap, the vacuum Rabi rate and the decoherence rate as function of the in-plane magnetic-field orientation. As the central result, we find a compromise-free sweet spot at which the qubit decoherence is minimal while simultaneously the qubit transition frequency and the dipolar coupling to the resonator are maximal. These experimental findings are well described by our theoretical model that shows that at the compromise-free sweet spot, the qubit is resilient against magnetic noise and phonon-mediated noise, with phonons forming the most likely dominant noise source.

Fitting the model, we find an anisotropic g-tensor with a maximal g-factor of $g_0 = 10.5$ and a spin-orbit length of $l_{\text{so}} = 120 \text{ nm}$, consistent with literature [9, 47]. Our findings demonstrate that, based on the magnetic field as global tuning parameter, optimization of speed and coherence are not mutually exclusive. Our experimental results and model are very generic and allow for further optimization through synthesis of specifically tailored composite crystals to suppress phonon-induced loss or through a larger resonator frequency. Sweet-spot operation might be crucial for larger qubit architectures and we anticipate that similar sweet-spots will be identified for other material platforms that rely on large spin-orbit interaction such as hole-spin qubits in Ge [8, 26, 65, 66].

VII. ACKNOWLEDGEMENTS

We are grateful for fruitful discussions with J. Danon, A. Ranni, C. Reissel and C. Ventura Meinersen. The research was supported by the Swiss Nanoscience Institute (SNI), and the Swiss National Science Foundation through grant 192027. This work was supported by the Swiss National Science Foundation, NCCR SPIN (grant number 51NF40-180604). We further acknowledge funding from the European Union's Horizon 2020 research and innovation programme, specifically the FET-open project AndQC, agreement No 828948 and the FET-open project TOPSQUAD, agreement No 847471. We also acknowledge support through the Marie Skłodowska -Curie COFUND grant QUSTEC, grant agreement N° 847471 and the Basel Quantum Center through a Georg H. Endress fellowship. We furthermore acknowledge support from NanoLund. P.S. acknowledges support from the Swiss National Science Foundation through Projects No. 200021_200418, and from the Swiss State Secretariat for Education, Research and Innovation (SERI) under contract number MB22.00081.

VIII. DATA AVAILABILITY

The numerical data used in this study are available in the zenodo database <https://doi.org/10.5281/zenodo.11205195>.

IX. METHODS

A. Device fabrication

The fabrication process commences with the sputter deposition of approximately 10 nm of NbTiN on a pristine Si/SiO₂ wafer [35]. Large structures are patterned utilizing a conventional e-beam protocol and developed at room temperature. Subsequently, the narrow resonator center conductor is patterned in a second e-beam step, followed by development at -20°C [67, 68]. Following

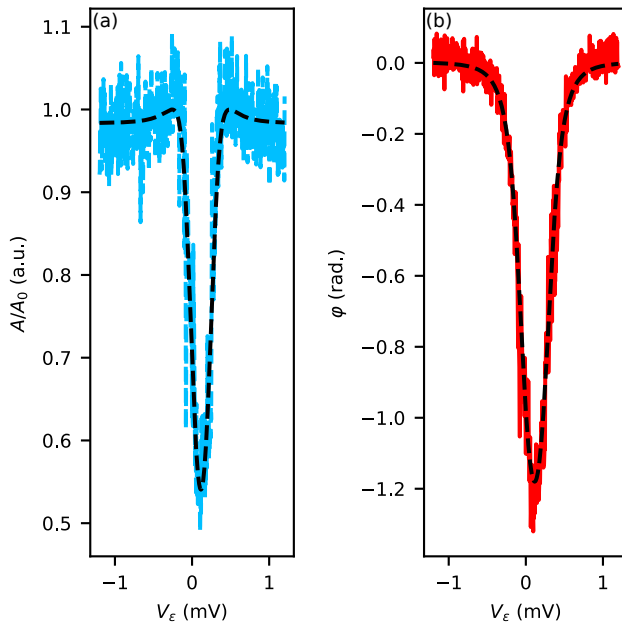


FIG. 5. **Linetrace with input-output theory fit at $\alpha = \pi/2$.** (a) Measured amplitude, A/A_0 , as a function of the virtual gate voltage, V_ϵ , along the detuning direction. (b) Measured phase φ as a function of detuning gate voltage V_ϵ . The data is a linecut of Fig. 3(a) at $\alpha = \pi/2$. The dashed curves are fits to Eq. (6)

the dry-etching of the NbTiN film, a NW is deterministically deposited using a micromanipulator. A GaSb-shell that is exclusively present on the zincblende segments of the NW [69, 70], allows us to identify the location of the wurtzite tunnel barriers using scanning electron microscopy. After identifying the tunnel barriers, the GaSb shell is removed by wet-etching in MF-319 developer [71]. Consecutively, the contacts and gates are patterned using standard e-beam lithography and thermal evaporation. For the contacts, Ar-milling in the evaporator ensures a good contact whereas the gates remain isolated by the native oxide on the NW.

B. Input-output theory

To determine the SOI gap Δ_{so} , the effective spin-photon coupling strength g_{eff} and the qubit decoherence rate γ , we make use of input-output theory that describes the interaction between photons in a resonator and a multi-level system [46, 72]. Input-output theory allows us to infer the transition frequency, vacuum Rabi rate and decoherence rate of two-level systems formed in a DQD [21, 22, 73–78]. For the singlet-triplet (S-T+) qubit coupled to a resonator, which is probed in transmission at low power, the linear response of the measured

scattering parameter is derived as [22, 79]

$$S_{21}(\omega) = \frac{-i\kappa}{\omega - \omega_0 + i\frac{\kappa}{2} - g^2 \left(\frac{1}{\omega - \omega_q + i\gamma} - \frac{1}{\omega + \omega_q + i\gamma} \right)}, \quad (6)$$

where $\omega_q = \sqrt{\Delta_{\text{so}}^2 + \varepsilon'^2}$, with $\varepsilon' = \varepsilon - \varepsilon_0$ the relative electrostatic DQD detuning from the center of the IDT and $g = g_{\text{eff}}\Delta_{\text{so}}/\omega_q$. Here we do not apply the usual rotating-wave approximation, preserving the counter-rotating terms, that are relevant for large frequency detuning $|\omega_q - \omega_0| \ll |\omega_q + \omega_0|$. To obtain the fit parameters plotted in Fig. 3(c), 3(d), and 3(e) for every value of field angle α , we fit amplitude and phase of Eq. (6) simultaneously to the measured amplitude and phase as a function of detuning ε . Fig. 5 shows amplitude and phase at $\alpha = \pi/2$ of the measurement shown in Fig. 3 with the overlaid fit. From this fit, we extract the SOI gap Δ_{so} , the coupling strength g_{eff} , and the decoherence rate γ . Repeating a similar procedure for various values of α results in the plots in Fig. 3 (c), (d) and (e). The resonator frequency ω_0 and resonator decay rate κ as well as the lever arm, transforming the applied gate voltages to detuning, are determined independently and kept fixed for the fit.

Resonator
Fluctuation amplitude, $\delta\varepsilon_0 = 0.6$
Spin-orbit tensor
Spin-orbit strength, $\Theta_{\text{so}} = d/l_{\text{so}} = 2.5$
in-plane angle, $\psi = 0.0 \text{ rad}$
Out-of-plane angle, $\Phi = 2.0 \text{ rad}$
g-tensor, g
Maximal g-factor, $g_0 = 10.5$
SOI correction, $\eta = 0.6$
In-plane angle, $\psi_g = 1.3 \text{ rad}$
Out-of-plane angle, $\Phi_g = 2.0 \text{ rad}$
Phonons
Phonon-mediated relaxation rate, $\Gamma_{\text{ph}}/2\pi = 160 \text{ GHz}$
Temperature, $T = 100 \text{ mK}$
Normalized speed of sound, $c_0 = c/(2\pi r) = (3 \text{ km s}^{-1})/(2\pi \cdot 50 \text{ nm})$
Normalized longitudinal wavefunction extend $l_0 = l/r = 200 \text{ nm}/50 \text{ nm}$
Normalized distance between wavefunctions $d_0 = d/r = 300 \text{ nm}/50 \text{ nm}$

TABLE I. Free parameters used to fit the data shown in Figure 3 of main text. The tunnel rate $t_c/2\pi = 4.5 \text{ GHz}$ as well as the gate-to-dot lever arms $\alpha_{L2} = 0.014 \pm 0.003$, $\alpha_{L1} = 0.044 \pm 0.008$, $\alpha_{R2} = 0.29 \pm 0.06$ and $\alpha_{R1} = 0.045 \pm 0.014$ were measured independently, where α_{ij} is the dimensionless lever arm between gate i and dot j . The spin-orbit strength Θ_{so} combined with the distance between the dots $d = 300 \text{ nm}$ (center to center) corresponds to a spin-orbit length $l_{\text{so}} = d/\Theta_{\text{so}} \approx 120 \text{ nm}$. The last three fit parameters are normalized by the wavefunction radius, $r = 50 \text{ nm}$.

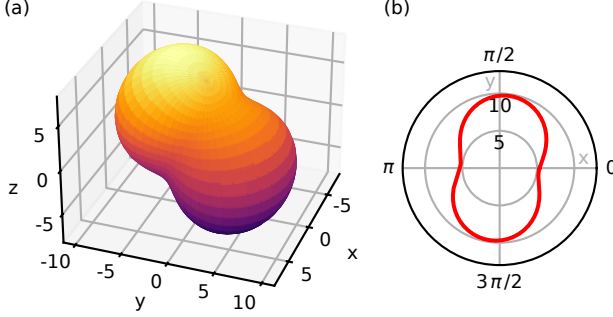


FIG. 6. **Visualization of the anisotropic g-tensor.** (a) Normalized Zeeman field strength $|Bg|/|B|$, where the g-tensor \underline{g} is defined according to Eq. (10). A characteristic peanut shape is exhibited. (b) Cross-section of (a) in the x - y plane at $z = 0$ as a function of the in-plane angle α . The nanowire is aligned parallel to the y axis.

C. Model of the double quantum dot

The curves plotted in Fig. 3 and 4 of the main text are the result of numerical diagonalization of the effective Hamiltonian of a double quantum dot (DQD) with even occupation close to the avoided crossing between $|T_{1,1}^+\rangle$ and $|S_{2,0}\rangle$. The $(1, 1) \rightarrow (0, 2)$ anticrossing is driven by changing the detuning ε between the two dots. For the usual negative exchange splitting between S and T states, the $(1, 1)$ state is preferred at $\varepsilon < 0$ and the state $(2, 0)$ is preferred at $\varepsilon > 0$.

The singlet and triplet states in the DQD are $(|S_{0,2}\rangle, |S_{2,0}\rangle, |S_{1,1}\rangle, |T_{1,1}^-\rangle, |T_{1,1}^+\rangle, |T_{1,1}^0\rangle)$ and form our basis set. The Hamiltonian including SOI then reads [24, 32, 80]

$$H_{\text{DQD}} = \begin{pmatrix} U_L + U_R + \varepsilon & U_{LR} & -t_c & 0 & 0 & 0 \\ U_{LR} & -\varepsilon & -t_c & 0 & 0 & 0 \\ -t_c & -t_c & -J_0 & -\frac{\delta b_x + i\delta b_y}{\sqrt{2}} & \frac{\delta b_x - i\delta b_y}{\sqrt{2}} & \delta b_z \\ 0 & 0 & -\frac{\delta b_x - i\delta b_y}{\sqrt{2}} & \bar{b}_z & 0 & \frac{\bar{b}_x - i\bar{b}_y}{\sqrt{2}} \\ 0 & 0 & \frac{\delta b_x + i\delta b_y}{\sqrt{2}} & 0 & -\bar{b}_z & \frac{\bar{b}_x + i\bar{b}_y}{\sqrt{2}} \\ 0 & 0 & \delta b_z & \frac{\bar{b}_x + i\bar{b}_y}{\sqrt{2}} & \frac{\bar{b}_x - i\bar{b}_y}{\sqrt{2}} & 0 \end{pmatrix}. \quad (7)$$

Here, $U_{L/R}$ is the on-site Coulomb energy of the left (L) and right (R) dot, U_{LR} is the cross-exchange contribution, and J_0 is the Coulomb exchange. And we define the difference and total Zeeman field vectors produced by a magnetic field \mathbf{B} as

$$\delta\mathbf{b} = \mu_B \mathbf{B} \delta g = \frac{\mu_B}{2} \mathbf{B} \left[\underline{g}_L \underline{R}(-\theta_{so}/2) - \underline{g}_R \underline{R}(\theta_{so}/2) \right], \quad (8)$$

$$\bar{\mathbf{b}} = \mu_B \mathbf{B} \bar{g} = \frac{\mu_B}{2} \mathbf{B} \left[\underline{g}_L \underline{R}(-\theta_{so}/2) + \underline{g}_R \underline{R}(\theta_{so}/2) \right], \quad (9)$$

where \underline{R} is a rotation matrix around the SOI axis by the spin-flip angle $\theta_{so} = d/l_{so}$, with d the distance between the dots and l_{so} the SOI length. For simplicity, we set $U_{LR} = J_0 = 0$. Following Ref. [32], we have gauged the spin-flip tunneling contribution into a local redefinition of the Zeeman energy and thus the tunneling amplitude t_c comprises both spin-conserving and spin-flip components. $\underline{g}_{L/R}$ are the g-tensors of the left and right dots, parameterized by the unit vector \mathbf{n} and the SOI correction factor $\eta \leq 1$,

$$\mathbf{B}g = g_0 [(\mathbf{n}(\mathbf{n} \cdot \mathbf{B})) + \eta(\mathbf{n} \times \mathbf{B}) \times \mathbf{n}]. \quad (10)$$

For describing the experimental results and to limit the number of free parameters, we use identical g-tensors for the left and right dot, $\underline{g} = \underline{g}_L = \underline{g}_R$.

The DQD is coupled to a resonator of frequency ω_0 and bosonic annihilation and creation operators a and a^\dagger , with the effective Hamiltonian $H_R = \hbar\omega_0 a^\dagger a$. The coupling is mediated by the resonator-induced change in detuning of the DQD and thus reads

$$H_I = \delta\varepsilon (|S_{20}\rangle\langle S_{20}| - |S_{02}\rangle\langle S_{02}|)(a^\dagger + a), \quad (11)$$

where $\delta\varepsilon = V_R \partial_V \varepsilon$ depends on the susceptibility of the detuning to the potential applied to the gate and on the zero-point-fluctuations V_R of the potential of the resonator.

Focusing on the $(1, 1) \rightarrow (0, 2)$ anticrossing at $\varepsilon \sim \varepsilon_0$, we neglect the contribution of the singlet $|S_{20}\rangle$ which lies at high energy $U_R + U_L$. We can then easily diagonalize the singlet subsector by accounting for the tunneling between S_{11} and S_{20} , and we focus on the 5 lowest energy states of the system, comprising the resulting singlets and the three triplets. The effective Hamiltonian reads

$$H_5 = \begin{pmatrix} J - \varepsilon & 0 & -\frac{(\delta b'_x + i\delta b'_y) \cos(\theta)}{\sqrt{2}} & \frac{(\delta b'_x - i\delta b'_y) \cos(\theta)}{\sqrt{2}} & \delta b'_z \cos(\theta) \\ 0 & -J & -\frac{(\delta b'_x + i\delta b'_y) \sin(\theta)}{\sqrt{2}} & \frac{(\delta b'_x - i\delta b'_y) \sin(\theta)}{\sqrt{2}} & \delta b'_z \sin(\theta) \\ -\frac{(\delta b'_x - i\delta b'_y) \cos(\theta)}{\sqrt{2}} & -\frac{(\delta b'_x - i\delta b'_y) \sin(\theta)}{\sqrt{2}} & E_z & 0 & 0 \\ \frac{(\delta b'_x + i\delta b'_y) \cos(\theta)}{\sqrt{2}} & \frac{(\delta b'_x + i\delta b'_y) \sin(\theta)}{\sqrt{2}} & 0 & -E_z & 0 \\ \delta b'_z \cos(\theta) & \delta b'_z \sin(\theta) & 0 & 0 & 0 \end{pmatrix}, \quad (12)$$

where $J \approx (\varepsilon + \sqrt{\varepsilon^2 + 4t_c^2})/2$ according to Eq. (1) and $\theta = \arctan(2t_c/\varepsilon)/2$, where the arctan function is defined, such that $\theta = \pi/4$ at $\varepsilon = 0$. We also fixed the direction of the spin quantization axis such that the triplet subsector is diagonal. This is done by defining the global rotation matrix \underline{R}_B that maps $\bar{\mathbf{b}}$ to the z -direction and rotating the $\delta\mathbf{b}$ accordingly, i.e.

$$\bar{\mathbf{b}} = E_z \underline{R}_B \mathbf{n}_z \rightarrow \delta\mathbf{b}' = \delta\mathbf{b} \underline{R}_B. \quad (13)$$

Here, \underline{R}_B depends on the direction of the applied \mathbf{B} field and on the combined g-tensor of the dots. The prime in $\delta\mathbf{b}'$ indicates this choice of reference frame for the spin quantization axis.

The resonator-DQD coupling Hamiltonian H_I in

Eq. (11) is related to variations in the detuning $\delta\epsilon$ by

$$H_I = \delta\epsilon_0 h_\varepsilon (a^\dagger + a), \quad (14)$$

with

$$h_\varepsilon = \begin{pmatrix} -\sin^2(\theta) & \sin(2\theta)/2 & 0 & 0 & 0 \\ \sin(2\theta)/2 & -\cos^2(\theta) & 0 & 0 & 0 \\ 0 & 0 & 0 & 0 & 0 \\ 0 & 0 & 0 & 0 & 0 \\ 0 & 0 & 0 & 0 & 0 \end{pmatrix} \quad (15)$$

describing small variations of the detuning ε . This leads to the definition of the dipolar coupling strength according to Eq. (4).

- [1] R. Hanson, L. P. Kouwenhoven, J. R. Petta, S. Tarucha, and L. M. K. Vandersypen, *Reviews of Modern Physics* **79**, 1217 (2007).
- [2] M. Veldhorst, J. C. C. Hwang, C. H. Yang, A. W. Leenstra, B. de Ronde, J. P. Dehollain, J. T. Muhonen, F. E. Hudson, K. M. Itoh, A. Morello, and A. S. Dzurak, *Nature Nanotechnology* **9**, 981 (2014).
- [3] J. Yoneda, T. Otsuka, T. Takakura, M. Pioro-Ladrière, R. Brunner, H. Lu, T. Nakajima, T. Obata, A. Noiri, C. J. Palmstrøm, A. C. Gossard, and S. Tarucha, *Applied Physics Express* **8**, 084401 (2015).
- [4] D. V. Bulaev and D. Loss, *Physical Review Letters* **95**, 076805 (2005).
- [5] D. V. Bulaev and D. Loss, *Physical Review Letters* **98**, 097202 (2007).
- [6] R. Maurand, X. Jehl, D. Kotekar-Patil, A. Corra, H. Boushlyskyi, R. Laviéville, L. Hutin, S. Barraud, M. Vinet, M. Sanquer, and S. De Franceschi, *Nature Communications* **7**, 13575 (2016).
- [7] H. Watzinger, J. Kukucka, L. Vukušić, F. Gao, T. Wang, F. Schäffler, J.-J. Zhang, and G. Katsaros, *Nature Communications* **9**, 3902 (2018).
- [8] F. N. Froning, L. C. Camenzind, O. A. van der Molen, A. Li, E. P. Bakkers, D. M. Zumbühl, and F. R. Braakman, *Nature Nanotechnology* **16**, 308 (2021).
- [9] S. Nadj-Perge, S. M. Frolov, E. P. a. M. Bakkers, and L. P. Kouwenhoven, *Nature* **468**, 1084 (2010).
- [10] M. D. Schroer, K. D. Petersson, M. Jung, and J. R. Petta, *Physical Review Letters* **107**, 176811 (2011).
- [11] K. D. Petersson, L. W. McFaull, M. D. Schroer, M. Jung, J. M. Taylor, A. A. Houck, and J. R. Petta, *Nature* **490**, 380 (2012).
- [12] I. van Weperen, B. Tarasinski, D. Eeltink, V. S. Pribiag, S. R. Plissard, E. P. A. M. Bakkers, L. P. Kouwenhoven, and M. Wimmer, *Physical Review B* **91**, 201413 (2015).
- [13] L. Han, M. Chan, D. De Jong, C. Prosko, G. Badawy, S. Gazibegovic, E. P. Bakkers, L. P. Kouwenhoven, F. K. Malinowski, and W. Pfaff, *Physical Review Applied* **19**, 014063 (2023).
- [14] E. Rashba and A. L. Efros, *Physical Review Letters* **91**, 126405 (2003).
- [15] V. N. Golovach, M. Borhani, and D. Loss, *Physical Review B* **74**, 165319 (2006).
- [16] K. C. Nowack, F. Koppens, Y. V. Nazarov, and L. Vandersypen, *Science* **318**, 1430 (2007).
- [17] J. Van den Berg, S. Nadj-Perge, V. Pribiag, S. Plissard, E. Bakkers, S. Frolov, and L. Kouwenhoven, *Physical Review Letters* **110**, 066806 (2013).
- [18] C. Kloeffel, M. Trif, P. Stano, and D. Loss, *Physical Review B* **88**, 241405 (2013).
- [19] A. Crippa, R. Ezzouch, A. Aprá, A. Amissé, R. Laviéville, L. Hutin, B. Bertrand, M. Vinet, M. Ur-dampilleta, T. Meunier, *et al.*, *Nature communications* **10**, 2776 (2019).
- [20] S. Bosco, P. Scarlino, J. Klinovaja, and D. Loss, *Physical Review Letters* **129**, 066801 (2022).
- [21] C. X. Yu, S. Zihlmann, J. C. Abadillo-Uriel, V. P. Michal, N. Rambal, H. Niebojewski, T. Bedecarrats, M. Vinet, E. Dumur, M. Filippone, B. Bertrand, S. De Franceschi, Y.-M. Niquet, and R. Maurand, *Nature Nanotechnology* **18**, 741 (2023), 2206.14082.
- [22] J. H. Ungerer, A. Pally, A. Kononov, S. Lehmann, J. Ridderbos, P. P. Potts, C. Thelander, K. A. Dick, V. F. Maisi, P. Scarlino, *et al.*, *Nature Communications* **15**, 1068 (2024).
- [23] F. De Palma, F. Oppliger, W. Jang, S. Bosco, M. Janík,

S. Calcaterra, G. Katsaros, G. Isella, D. Loss, and P. Scarlino, arXiv:2310.20661 (2023).

[24] D. Stepanenko, M. Rudner, B. I. Halperin, and D. Loss, *Physical Review B* **85**, 075416 (2012).

[25] J. M. Nichol, S. P. Harvey, M. D. Shulman, A. Pal, V. Umansky, E. I. Rashba, B. I. Halperin, and A. Yacoby, *Nature Communications* **6**, 7682 (2015).

[26] D. Jirovec, A. Hofmann, A. Ballabio, P. M. Mutter, G. Tavani, M. Botifoll, A. Crippa, J. Kukucka, O. Sagi, F. Martins, *et al.*, *Nature Materials* **20**, 1106 (2021).

[27] N. Samkharadze, G. Zheng, N. Kalhor, D. Brousse, A. Sammak, U. Mendes, A. Blais, G. Scappucci, and L. Vandersypen, *Science* **359**, 1123 (2018).

[28] X. Mi, M. Benito, S. Putz, D. M. Zajac, J. M. Taylor, G. Burkard, and J. R. Petta, *Nature* **555**, 599 (2018).

[29] A. J. Landig, J. V. Koski, P. Scarlino, U. C. Mendes, A. Blais, C. Reichl, W. Wegscheider, A. Wallraff, K. Ensslin, and T. Ihn, *Nature* **560**, 179 (2018).

[30] N. Piot, B. Brun, V. Schmitt, S. Zihlmann, V. Michal, A. Apra, J. Abadillo-Uriel, X. Jehl, B. Bertrand, H. Niebojewski, *et al.*, *Nature Nanotechnology* **17**, 1072 (2022).

[31] S. d'Hollosy, G. Fábián, A. Baumgartner, J. Nygård, and C. Schönenberger, in *AIP Conference Proceedings*, Vol. 1566 (American Institute of Physics, 2013) pp. 359–360.

[32] S. Geyer, B. Hetényi, S. Bosco, L. C. Camenzind, R. S. Eggli, A. Fuhrer, D. Loss, R. J. Warburton, D. M. Zumbühl, and A. V. Kuhlmann, *Nature Physics* **1**, 1 (2024).

[33] M. J. Carballido, S. Svab, R. S. Eggli, T. Patlatiuk, P. C. Kwon, J. Schuff, R. M. Kaiser, L. C. Camenzind, A. Li, N. Ares, *et al.*, arXiv:2402.07313 (2024).

[34] N. Samkharadze, A. Bruno, P. Scarlino, G. Zheng, D. P. DiVincenzo, L. DiCarlo, and L. M. K. Vandersypen, *Physical Review Applied* **5**, 044004 (2016).

[35] J. H. Ungerer, D. Sarmah, A. Kononov, J. Ridderbos, R. Haller, L. Y. Cheung, and C. Schönenberger, *EPJ Quantum Technology* **10**, 1 (2023).

[36] S. Lehmann, J. Wallentin, D. Jacobsson, K. Deppert, and K. A. Dick, *Nano Letters* **13**, 4099 (2013).

[37] M. Nilsson, L. Namazi, S. Lehmann, M. Leijnse, K. A. Dick, and C. Thelander, *Physical Review B* **93**, 195422 (2016).

[38] T. Tanttu, B. Hensen, K. W. Chan, C. H. Yang, W. W. Huang, M. Fogarty, F. Hudson, K. Itoh, D. Culcer, A. Laucht, *et al.*, *Physical Review X* **9**, 021028 (2019).

[39] C. Jünger, R. Delagrange, D. Chevallier, S. Lehmann, K. A. Dick, C. Thelander, J. Klinovaja, D. Loss, A. Baumgartner, and C. Schönenberger, *Physical Review Letters* **125**, 017701 (2020).

[40] A. Stockklauser, P. Scarlino, J. V. Koski, S. Gasparinetti, C. K. Andersen, C. Reichl, W. Wegscheider, T. Ihn, K. Ensslin, and A. Wallraff, *Physical Review X* **7**, 011030 (2017).

[41] M. Schroer, M. Jung, K. Petersson, and J. R. Petta, *Physical Review Letters* **109**, 166804 (2012).

[42] F. K. Malinowski, F. Martins, T. B. Smith, S. D. Bartlett, A. C. Doherty, P. D. Nissen, S. Fallahi, G. C. Gardner, M. J. Manfra, C. M. Marcus, *et al.*, *Physical Review X* **8**, 011045 (2018).

[43] R. Ezzouch, S. Zihlmann, V. P. Michal, J. Li, A. Aprá, B. Bertrand, L. Hutin, M. Vinet, M. Urdampilleta, T. Meunier, *et al.*, *Physical Review Applied* **16**, 034031 (2021).

[44] T. Frey, P. J. Leek, M. Beck, A. Blais, T. Ihn, K. Ensslin, and A. Wallraff, *Physical Review Letters* **108**, 046807 (2012).

[45] N. Hendrickx, L. Massai, M. Mergenthaler, F. Schupp, S. Paredes, S. Bedell, G. Salis, and A. Fuhrer, arXiv:2305.13150 (2023).

[46] C. W. Gardiner and M. J. Collett, *Physical Review A* **31**, 3761 (1985).

[47] C. Fasth, A. Fuhrer, L. Samuelson, V. N. Golovach, and D. Loss, *Physical Review Letters* **98**, 266801 (2007).

[48] L. V. Assali, H. M. Petrilli, R. B. Capaz, B. Koiller, X. Hu, and S. D. Sarma, *Physical Review B* **83**, 165301 (2011).

[49] J. Schliemann, A. Khaetskii, and D. Loss, *Journal of Physics: Condensed Matter* **15**, R1809 (2003).

[50] C. Testelin, F. Bernardot, B. Eble, and M. Chamarro, *Physical Review B* **79**, 195440 (2009).

[51] K. Petersson, J. Petta, H. Lu, and A. Gossard, *Physical Review Letters* **105**, 246804 (2010).

[52] N. Holman, D. Rosenberg, D. Yost, J. Yoder, R. Das, W. D. Oliver, R. McDermott, and M. Eriksson, *npj Quantum Information* **7**, 137 (2021).

[53] E. Paladino, Y. Galperin, G. Falci, and B. Altshuler, *Reviews of Modern Physics* **86**, 361 (2014).

[54] P. Scarlino, J. H. Ungerer, D. J. van Woerkom, M. Mancini, P. Stano, C. Müller, A. J. Landig, J. V. Koski, C. Reichl, W. Wegscheider, *et al.*, *Physical Review X* **12**, 031004 (2022).

[55] T. Fujisawa, T. H. Oosterkamp, W. G. Van der Wiel, B. W. Broer, R. Aguado, S. Tarucha, and L. P. Kouwenhoven, *Science* **282**, 932 (1998).

[56] V. N. Golovach, A. Khaetskii, and D. Loss, *Physical Review Letters* **93**, 016601 (2004).

[57] M. Trif, V. N. Golovach, and D. Loss, *Physical Review B* **77**, 045434 (2008).

[58] V. Kornich, C. Kloeffel, and D. Loss, *Physical Review B* **89**, 085410 (2014).

[59] C. Kloeffel, M. Trif, and D. Loss, *Physical Review B* **90**, 115419 (2014).

[60] V. Kornich, C. Kloeffel, and D. Loss, *Quantum* **2**, 70 (2018).

[61] T. Hartke, Y.-Y. Liu, M. Gullans, and J. Petta, *Physical Review Letters* **120**, 097701 (2018).

[62] A. Hofmann, C. Karlewski, A. Heimes, C. Reichl, W. Wegscheider, G. Schön, K. Ensslin, T. Ihn, and V. F. Maisi, *Physical Review Research* **2**, 033230 (2020).

[63] J. Zou, S. Bosco, and D. Loss, *npj Quantum Information* **10**, 46 (2024).

[64] L. Cywiński, R. M. Lutchyn, C. P. Nave, and S. D. Sarma, *Physical Review B* **77**, 174509 (2008).

[65] N. Hendrickx, W. Lawrie, L. Petit, A. Sammak, G. Scappucci, and M. Veldhorst, *Nature communications* **11**, 3478 (2020).

[66] X. Zhang, E. Morozova, M. Rimbach-Russ, D. Jirovec, T.-K. Hsiao, P. C. Fariña, C.-A. Wang, S. D. Oosterhout, A. Sammak, G. Scappucci, *et al.*, arXiv:2312.16101 (2023).

[67] J. Ridderbos, *Quantum dots and superconductivity in Ge-Si nanowires*, Ph.D. thesis, University of Twente (2018).

[68] J. H. Ungerer, *High-impedance circuit quantum electrodynamics with semiconductor quantum dots*, Ph.D. thesis, University of Basel (2023).

[69] C. Gatzke, S. Webb, K. Fobelets, and R. Stradling, *Semiconductor science and technology* **13**, 399 (1998).

- [70] D. Barker, S. Lehmann, L. Namazi, M. Nilsson, C. Thelander, K. A. Dick, and V. F. Maisi, *Applied Physics Letters* **114** (2019).
- [71] A. P. Pally, *Crystal-phase defined nanowire quantum dots as a platform for qubits*, Ph.D. thesis, University of Basel (2024).
- [72] M. Benito, X. Mi, J. M. Taylor, J. R. Petta, and G. Burkard, *Physical Review B* **96**, 235434 (2017).
- [73] G. Burkard and J. R. Petta, *Physical Review B* **94**, 195305 (2016).
- [74] X. Mi, C. G. Péterfalvi, G. Burkard, and J. R. Petta, *Physical Review Letters* **119**, 176803 (2017).
- [75] F. Borjans, X. Zhang, X. Mi, G. Cheng, N. Yao, C. Jackson, L. Edge, and J. Petta, *PRX Quantum* **2**, 020309 (2021).
- [76] D. J. Ibberson, T. Lundberg, J. A. Haigh, L. Hutin, B. Bertrand, S. Barraud, C.-M. Lee, N. A. Stelmashenko, G. A. Oakes, L. Cochrane, *et al.*, *PRX Quantum* **2**, 020315 (2021).
- [77] M. J. Ruckriegel, L. M. Gächter, D. Kealhofer, M. B. Panah, C. Tong, C. Adam, M. Masseroni, H. Duprez, R. Garreis, K. Watanabe, *et al.*, arXiv:2312.14629 (2023).
- [78] A. Ranni, S. Haldar, H. Havar, S. Lehmann, P. Scarlino, A. Baumgartner, C. Schönenberger, C. Thelander, K. A. Dick, P. P. Potts, *et al.*, arXiv:2308.14887 (2023).
- [79] S. Kohler, *Physical Review A* **98**, 023849 (2018).
- [80] M. Spethmann, S. Bosco, A. Hofmann, J. Klinovaja, and D. Loss, *Physical Review B* **109**, 085303 (2024).

Supplementary Material – A coherence sweet spot with enhanced dipolar coupling

J. H. Ungerer,^{1, 2, 3,*} A. Pally,^{2, †} S. Bosco,⁴ A. Kononov,² D. Sarmah,² S. Lehmann,⁵ C. Thelander,⁵ V.F. Maisi,⁵ P. Scarlino,⁶ D. Loss,² A. Baumgartner,^{1, 2} and C. Schönenberger^{1, 2, ‡}

¹Swiss Nanoscience Institute, University of Basel, Klingelbergstrasse 82 CH-4056, Switzerland

²Department of Physics, University of Basel, Klingelbergstrasse 82 CH-4056, Switzerland

³Department of Physics, Harvard University, Cambridge, MA 02138, USA

⁴QuTech and Kavli Institute of Nanoscience, Delft University of Technology, Lorentzweg 1, 2628 CJ Delft, Netherlands

⁵Solid State Physics and NanoLund, Lund University, Box 118, S-22100 Lund, Sweden

⁶Institute of Physics and Center for Quantum Science and Engineering,
Ecole Polytechnique Fédérale de Lausanne, CH-1015 Lausanne, Switzerland

(Dated: May 20, 2024)

In this supplementary, we discuss in detail the relevant theoretical considerations about the possible sources of decoherence that might give rise to the experimentally observed compromise-free sweet spot described in the main text.

I. GENERAL FRAMEWORK FOR DECOHERENCE

In this Supplementary Material (SM), we investigate several possible origins of noise in order to pinpoint to the dominant noise source explaining the dependence of the experimentally measured decoherence. The investigate the decoherence of the ST transition, which consists in dephasing and relaxation,

$$\gamma = \frac{\gamma_1}{2} + \gamma_\varphi . \quad (1)$$

Generally for a two-level transition, we can model the noise by the effective Hamiltonian

$$H_N^D = \delta_z \frac{\tau_z}{2} + \delta_x \frac{\tau_x}{2} + \delta_y \frac{\tau_y}{2} , \quad (2)$$

where the index D indicates that we are working in the diagonal basis of the two-level system, gapped by the energy Δ_{so} . The first term in H_N^D causes pure dephasing (with decoherence rate γ_φ), while the second and third are responsible for relaxation (with rate γ_1).

By following Bloch-Redfield theory [1, 2], we find

$$\gamma_1 = \frac{1}{2\hbar^2} \int_{-\infty}^{\infty} d\tau \cos\left(\frac{\Delta_{\text{so}}\tau}{\hbar}\right) \left(\langle \delta_x(0)\delta_x(\tau) \rangle + \langle \delta_y(0)\delta_y(\tau) \rangle \right) , \quad (3)$$

$$\gamma_\varphi = \frac{1}{2\hbar^2} \int_{-\infty}^{\infty} d\tau \langle \delta_z(0)\delta_z(\tau) \rangle . \quad (4)$$

Here, $\langle O(0)O(\tau) \rangle$ is the correlator of the operator O , typically evaluated for baths at thermal equilibrium. One can simplify these equations by introducing the spectral function of the noise

$$S_{ij}(\hbar\omega) = \int_{-\infty}^{\infty} d\tau e^{-i\omega\tau} \langle \delta_i(0)\delta_j(\tau) \rangle , \quad \langle \delta_i(0)\delta_j(\tau) \rangle = \frac{1}{2\pi} \int_{-\infty}^{\infty} d\omega e^{i\omega\tau} S_{ij}(\hbar\omega) , \quad (5)$$

resulting in

$$\gamma_1 = \frac{S_{xx}(-\Delta_{\text{so}}) + S_{yy}(-\Delta_{\text{so}}) + S_{xx}(\Delta_{\text{so}}) + S_{yy}(\Delta_{\text{so}})}{4\hbar^2} \quad (6)$$

$$\gamma_\varphi = \frac{S_{zz}(0)}{2\hbar^2} . \quad (7)$$

* Equal contributions.; jungerer@g.harvard.edu

† Equal contributions.

‡ nanoelectronics.unibas.ch

Note that one can estimate the effect of pure dephasing better by employing the filter function formalism, following Ref. [3]. For Gaussian noise and free induction decay, one finds that the decay of coherence is not generally exponential $e^{-t\gamma_\varphi}$, but follows the law

$$\exp \left[-\frac{1}{\pi \hbar^2} \int_{-\infty}^{\infty} d\omega S_{zz}(\hbar\omega) \frac{\sin^2(\omega t/2)}{\omega^2} \right], \quad (8)$$

and agrees exactly with the result above (and with the exponential decay) for white noise $S_{zz}(\hbar\omega) \rightarrow S_{zz}(0)$.

We now adapt this theory to describe some possible mechanisms that produce noise in the system.

II. TUNNELING AND DETUNING NOISE

Here, we explicitly calculate the decoherence for several noise sources, investigating whether the trend in γ matches with the experimentally measured values. While doing so, we amplify the noise by a factor that might be reasonable depending on experimental circumstances. This allows us to exclude the particular noise source as dominant, if the trend does not match.

A possible decoherence mechanism is the coupling of charge traps and phonons to the tunneling and detuning of the DQD. The noise in this section is computed as follows: We first find the eigenstates of the DQD Hamiltonian in Eq. 13 of the main text. These eigenstates depend on B field amplitude and direction, as well as on detuning. Then we project the vairiaion of tunnelling and detuning (put in the equations 15 and 16 from Cleaner notes, and add the prefactor delta t(t) and delta epsilon (t))) onto these eigenstates. Restricting ourselves to the subspace spanned by the ground and first excited state, we find the Hamiltonain in Eq. (2) and the dependence of the coupling to the noise sources δ_t and δ_ϵ on detuning and B field. We then find the values at the anticrossing by evaluating at detuning values such that $\partial_\epsilon(E_1 - E_0) = 0$. We neglect here the possible coupling of noise directly to the spin degree of freedom that might occur via an electric field tunable g-tensor and spin-orbit interaciton.

A. 1/f charge noise

We consider the effect of an ensemble of random charge fluctuators coupling to the DQD. These impurities cause flucutations of the electrostatic potential V that then couple to both t_c and ϵ , and typically results in the noise spectrum

$$S_{tt}(\omega) = \int d\tau e^{-i\omega\tau} \langle \delta_t(0)\delta_t(\tau) \rangle \quad (9)$$

$$= \left(\frac{\partial t}{\partial V} \right)^2 \bar{V}^2 \frac{\omega_0^{\alpha-1}}{|\omega|^\alpha}, \quad (10)$$

$$S_{\epsilon\epsilon}(\omega) = \int d\tau e^{-i\omega\tau} \langle \delta_\epsilon(0)\delta_\epsilon(\tau) \rangle \quad (11)$$

$$= \left(\frac{\partial \epsilon}{\partial V} \right)^2 \bar{V}^2 \frac{\omega_0^{\alpha-1}}{|\omega|^\alpha}, \quad (12)$$

with $\alpha \in (0, 2]$, $\omega_0 = 2\pi$ Hz being a reference frequency, and $\bar{V} \sim \mu\text{eV}$ characterizing the amplitude of the noise.

Using these noise spectra, we numerically calculate the relaxation rates and dephasing rates due to noise coupling via the detuning and tunneling and plot the results in Figure 1. The operators describing small variations of tunelling t_c and detuning ϵ are given by

$$h_{\delta t} = \begin{pmatrix} \sin(2\theta) & -\cos(2\theta) & 0 & 0 & 0 \\ -\cos(2\theta) & -\sin(2\theta) & 0 & 0 & 0 \\ 0 & 0 & 0 & 0 & 0 \\ 0 & 0 & 0 & 0 & 0 \\ 0 & 0 & 0 & 0 & 0 \end{pmatrix}, \quad (13)$$

$$h_\epsilon = \begin{pmatrix} -\sin^2(\theta) & \sin(2\theta)/2 & 0 & 0 & 0 \\ \sin(2\theta)/2 & -\cos^2(\theta) & 0 & 0 & 0 \\ 0 & 0 & 0 & 0 & 0 \\ 0 & 0 & 0 & 0 & 0 \\ 0 & 0 & 0 & 0 & 0 \end{pmatrix}. \quad (14)$$

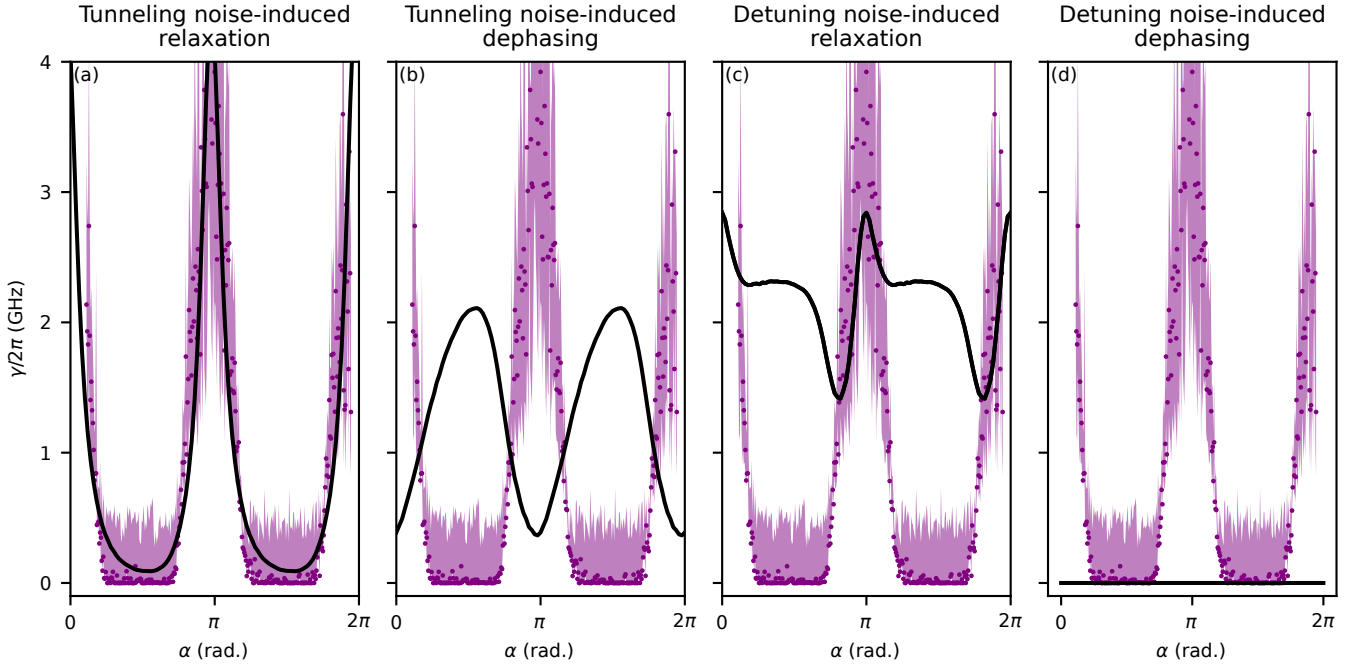


FIG. 1. **Pink (1/f) noise.** All subfigures show the experimental data for the total dephasing rates (purple). The overlaid curves are (a) Black curve represents the relaxation rate due to pink noise coupling to the tunnel rate, $\gamma_1^{t,1/f} = \frac{|h_{\delta t 01}|^2 S_{tt}(\Delta_{\text{so}})}{4\hbar^2}$. (b) Black curve represents the dephasing due to pink noise coupling to the tunnel rate t_c , $\gamma_\varphi^{t,1/f} = \sqrt{2 \cdot 3.5} (\langle 0 | h_{\delta t} | 0 \rangle - \langle 1 | h_{\delta t} | 1 \rangle)$. (c) Black curve represents the relaxation due to pink noise coupling to the detuning ε , $\gamma_1^\varepsilon = \frac{|h_{\delta \varepsilon 01}|^2 S_{\varepsilon \varepsilon}(\Delta_{\text{so}})}{4\hbar^2}$. (d) Black curve represents the dephasing due to pink noise coupling to the detuning ε , $\gamma_\varphi^\varepsilon = 0$. This term vanishes because it was evaluated at the avoided crossing, where $\partial(E_1 - E_0)/\partial\varepsilon = 0$.

The definitions of these operators leads to the matrix elements

$$h_{\delta t 01} = \langle 0 | h_{\delta t} | 1 \rangle, h_{\delta t z} = \frac{\langle 0 | h_{\delta t} | 0 \rangle - \langle 1 | h_{\delta t} | 1 \rangle}{2}, h_{\delta \varepsilon 01} = \langle 0 | h_{\delta \varepsilon} | 1 \rangle, h_{\delta \varepsilon z} = \frac{\langle 0 | h_{\delta \varepsilon} | 0 \rangle - \langle 1 | h_{\delta \varepsilon} | 1 \rangle}{2}, \quad (15)$$

where $|0\rangle$ and $|1\rangle$ are the qubit states. We note that, by construction, noise coupling via the detuning ε does not cause dephasing because the noise is evaluated at the position of the avoided crossing where $\partial_\varepsilon(E_1 - E_0) = 0$. The relaxation rate due to pink noise coupling to the tunnel rate is then given by,

$$\gamma_1^{t,1/f} = \frac{|h_{\delta t 01}|^2 S_{tt}(\Delta_{\text{so}})}{4\hbar^2} \quad (16)$$

and the relaxation due to pink noise coupling via the detuning reads

$$\gamma_1^\varepsilon = \frac{|h_{\delta \varepsilon 01}|^2 S_{\varepsilon \varepsilon}(\Delta_{\text{so}})}{4\hbar^2}. \quad (17)$$

We then estimate the decay as Gaussian (see Eq. (8)), rather than exponential. Neglecting log corrections leads to the dephasing due to pink noise coupling to the tunnel rate

$$\gamma_\varphi^{t,1/f} \approx \frac{1}{\hbar} |h_{\delta t z}| \bar{V} \frac{dt}{dV}, \quad (18)$$

and the dephasing due to pink noise coupling to the detuning

$$\gamma_\varphi^{\varepsilon,1/f} \approx \frac{1}{\hbar} |h_{\delta \varepsilon z}| \bar{V} \frac{d\varepsilon}{dV}. \quad (19)$$

These quantities from Eqs. (16), (17), (18) and (19) are plotted as curves overlaid over the decoherence rate extracted from the measurements in Fig. 1. From the curves, it becomes obvious that when considering pink noise, only

relaxation due to coupling via the tunnel rate t_c results in the trend that is observed in the experimental data. However, if this was the main source of noise, the total decoherence rate would be the sum of the the dephasing and the relaxation terms (Fig. 1(a) and (b), thus providing a globally different trend than what observed in the experiment.

B. Phonons

We consider two types of phonon interactions, whose energy is determined by their strain tensor ε . Deformational phonon interactions create a potential via longitudinal terms in the strain tensor

$$H_D = \varepsilon_D \text{Tr}(\varepsilon) , \quad (20)$$

while piezoelectric phonon interactions introduce in the system an electric field \mathbf{E}_s via the shear strain tensor elements, which results in

$$H_P = -e \int d\mathbf{r}' \frac{(\nabla \cdot \mathbf{E}_s)(\mathbf{r}')}{|\mathbf{r} - \mathbf{r}'|} , \quad (21)$$

$$\mathbf{E}_s = E_P \begin{pmatrix} \varepsilon_{yz} \\ \varepsilon_{xz} \\ \varepsilon_{xy} \end{pmatrix} . \quad (22)$$

We ignore here the vector potential contributions of \mathbf{E}_s . The energy $\varepsilon_D \sim 14$ eV, and the piezoelectric electric field $E_P \sim 0.1$ V/nm are material-dependent parameters.

The tunneling and detuning fluctuations caused by these phonons are then given by

$$\delta t_{D,P} = 2\langle \Psi_L | H_{D,P} | \Psi_R \rangle , \quad \delta \varepsilon_{D,P} = \langle \Psi_L | H_{D,P} | \Psi_L \rangle - \langle \Psi_R | H_{D,P} | \Psi_R \rangle , \quad (23)$$

where $|\Psi_{L,R}\rangle$ are the orthonormalized electronic wavefunctions of the left and right dots. We note that here $\delta t_{D,P}$ and $\delta \varepsilon_{D,P}$ are operators and thus the phonons spectral function is generally asymmetric in frequency, causing quantum noise (see e.g. Ref. [4]). Moreover, because the phonons spectral function vanishes at $\omega = 0$, we restrict ourselves to the analysis of the dominant contribution of phonons to decoherence that is relaxation.

We also focus on the tunneling and detuning flucutations caused by phonons confined in a 1 dimensional nanowire. We consider here a simplified model of the nanowire based on continuous elasticity theory in isotropic medium, which assumed the wire to be infinitely long (formally with a length $L \rightarrow \infty$) and cylindrical with radius R . There are four phonon modes: longitudinal, transversal, and two flexural modes. The longitudinal mode contributes via both piezoelectric and deformational interactions, while the others only via piezoelectric ones.

However, by following closely Ref. [5], we find that the shear strain components ε_{ij} of the different modes oscillate around the nanowire and thus their contribution averages to zero if the electronic wavefunction is cylindrical. These interactions qualitatively capture the trends observed in experiment. We note that piezoelectric phonon coupling vanishes in our simplified model, but it can still be quantitatively relevant in experiments if one includes non-cylydnrical and finite length nanowires and anisotropic elastic media. We also neglect here the effect of the difference of materials in the wire, which could have an effect to modify the phonon-quibit itneractions. For this reason, we expect that the dominant contribution of the phonons is caused by longitudinal phonon modes coupled via deformational interactions.

Assuming the electronic wavefunctions to be Gaussians of width l , shifted by a distance d , orthonomalized as

$$\begin{pmatrix} \langle \mathbf{r} | \Psi_R \rangle \\ \langle \mathbf{r} | \Psi_L \rangle \end{pmatrix} = \frac{e^{-(x^2+y^2)/2R^2}}{\sqrt{\pi}R} \frac{1}{2\sqrt[4]{\pi}l^2} \begin{pmatrix} \frac{1}{\sqrt{1+s}} + \frac{1}{\sqrt{1-s}} & \frac{1}{\sqrt{1+s}} - \frac{1}{\sqrt{1-s}} \\ \frac{1}{\sqrt{1+s}} - \frac{1}{\sqrt{1-s}} & \frac{1}{\sqrt{1+s}} + \frac{1}{\sqrt{1-s}} \end{pmatrix} \begin{pmatrix} e^{-(z-d)^2/2l^2} \\ e^{-(z+d)^2/2l^2} \end{pmatrix} , \quad (24)$$

with $s = e^{-d^2/l^2}$, we obtain from Eq. (23) [and using Eqs. (78)-(80) and (98) in Ref. [5]]

$$\delta \varepsilon_D = \varepsilon_D (1 - 2\nu) \frac{1}{\sqrt{1 - e^{-2d^2/l^2}}} \sum_q \sqrt{\frac{2\hbar}{\pi L R^4 \rho c_l |q|}} |q| Re^{-q^2 l^2/4} \sin(|q|d) [a_q^\dagger + a_q] , \quad (25)$$

$$\delta t_D = \varepsilon_D (1 - 2\nu) \text{csch} \left(\frac{d^2}{l^2} \right) \sum_q \sqrt{\frac{2\hbar}{\pi L R^4 \rho c_l |q|}} |q| Re^{-q^2 l^2/4} \sin^2 \left(\frac{|q|d}{2} \right) [a_q^\dagger + a_q] , \quad (26)$$

which results in the relaxation time

$$\gamma_1^{ph} = \gamma_1^\epsilon + \gamma_1^t \quad (27)$$

$$\gamma_1^i = \Gamma_{ph} |h_{\delta i 01}|^2 \coth \left(\frac{\Delta_{so}}{2\hbar k T} \right) F_i \left(\frac{\Delta_{so}}{\hbar c_l} \right), \quad (28)$$

$$F_\varepsilon(q) = |q| Re^{-q^2 l^2/2} \frac{1}{1 - e^{-2d^2/l^2}} \sin^2(|q|d), \quad (29)$$

$$F_t(q) = |q| Re^{-q^2 l^2/2} \operatorname{csch}^2 \left(\frac{d^2}{l^2} \right) \sin^4 \left(\frac{|q|d}{2} \right). \quad (30)$$

Here, $c_l \approx 3 \times 10^3$ m/s is the phase velocity of the longitudinal phonons with wavevector q , $\rho = 5.5$ g/cm³ is the density, and $\nu = 0.3$ is the Poisson ratio. We assumed that the phonons are in a thermal state with temperature T . When evaluating the expectation values of the phonon operators, we used $\langle a_q^\dagger a_{q'} \rangle = \delta_{qq'} N(\omega_q)$, $\langle a_q a_{q'}^\dagger \rangle = \delta_{qq'} [1 + N(\omega_q)]$ [with $N(x) = 1/(e^{\hbar x/k_B T} - 1)$], and $a_q^\dagger(\tau) = a_q^\dagger e^{i\omega_q \tau}$, $a_q(\tau) = a_q e^{-i\omega_q \tau}$. We also made use of the equality $1 + 2N(x) = \coth(\hbar x/2k_B T)$, and we converted the sum over discrete momenta to the integral $\int dq L/(2\pi)$. The coupling to detuning and tunnelling are related to the decoherence of the qubit by the procedure discussed above, which involves the projection of $h_{\delta t}$ and $h_{\delta \epsilon}$ hamiltonian to the qubit subspace. We note that the phonon-mediated relaxation rate Γ_{ph} can be estimated as

$$\Gamma_D = \frac{\varepsilon_D^2 (1 - 2\nu)^2}{2\pi\hbar R^3 \rho c_l^2} \approx 200 \text{ MHz}, \quad (31)$$

when $R \sim 50$ nm. This is consistent with previous estimations [6] and in reasonable agreements with charge-like experiments in a similar device.

The theoretical curves in Fig. 3(e) and Fig. 4(a) corespond to Eq. (28) with numerically calculated matrix elements $|h_{\delta \varepsilon 01}(\alpha)|$, $|h_{\delta t_c 01}(\alpha)|$. To plot the curve plotted in Fig. 4(b), we fix $|h_{\delta \varepsilon 01}| = |h_{\delta t_c 01}| = 0.7$ to derive an analytical equation $\gamma_1^{ph}(\omega)$. While the trend captured by the phonon dispersion nicely reproduces the features observed in the experiment, we note that $\Gamma_{ph} = 240$ GHz, extracted from our measurement, and setting the largest decay rate, is significantly larger than Γ_D . This discrepancy could be due to the physical structure of the nanowire, for example the tunnel barrier between the two dots could modify the phonon-qubit coupling. Also, the non-perfectly one-dimensional nature of the wire could be relevant. Another possibility to explain the larger Γ_D is that, we are close to a phonon-relaxation hotspot, that can arise at the frequencies where higher phonon modes become populated. We estimate that the higher modes become populated at frequencies $\sim c_l/2R \sim 30$ GHz [6], not too far from the values of Δ_{so} in our experiment. Fig. 2 shows the relaxation caused by phonons. Fig. 2(a) is equivalent to Fig. 3(e) and Fig. 4(a) in the main text and shows the relaxation mediated by phonons coupling to the tunneling. Fig. 2(b) shows the phonon-induced relaxation due to coupling via the detuning. We speculate that the the fact that the barriers are built of wurtzite InAs, compared to the zincblende InAs quantum dots, results in large phonon-induced variations of the tunnel coupling.

III. NUCLEAR SPIN NOISE

We consider magnetic noise, such as nuclear spin noise, as source of decoherence. To model this noise source, we introduce here the fluctuations $\delta \mathbf{B}_N^{L,R}$ of the magnetic field in the left and right dots, which result in

$$\delta \mathbf{b}^N = \frac{\mu_B}{2} \left[\delta \mathbf{B}_N^L \underline{g}_L R(-\theta_{so}/2) - \delta \mathbf{B}_N^R \underline{g}_R R(\theta_{so}/2) \right], \quad (32)$$

$$\bar{\mathbf{b}}^N = \frac{\mu_B}{2} \left[\delta \mathbf{B}_N^L \underline{g}_L R(-\theta_{so}/2) + \delta \mathbf{B}_N^R \underline{g}_R R(\theta_{so}/2) \right], \quad (33)$$

and produce the magnetic noise Hamiltonian

$$H_M = \begin{pmatrix} 0 & 0 & \frac{-(\delta b_x^N + i\delta b_y^N) \cos(\theta)}{\sqrt{2}} & \frac{(\delta b_x^N - i\delta b_y^N) \cos(\theta)}{\sqrt{2}} & \delta b_z^N \cos(\theta) \\ 0 & 0 & \frac{-(\delta b_x^N + i\delta b_y^N) \sin(\theta)}{\sqrt{2}} & \frac{(\delta b_x^N - i\delta b_y^N) \sin(\theta)}{\sqrt{2}} & \delta b_z^N \sin(\theta) \\ \frac{-(\delta b_x^N - i\delta b_y^N) \cos(\theta)}{\sqrt{2}} & \frac{-(\delta b_x^N - i\delta b_y^N) \sin(\theta)}{\sqrt{2}} & \bar{b}_z^N & 0 & \frac{\bar{b}_x^N - i\bar{b}_y^N}{\sqrt{2}} \\ \frac{(\delta b_x^N + i\delta b_y^N) \cos(\theta)}{\sqrt{2}} & \frac{(\delta b_x^N + i\delta b_y^N) \sin(\theta)}{\sqrt{2}} & 0 & -\bar{b}_z^N & \frac{\bar{b}_x^N + i\bar{b}_y^N}{\sqrt{2}} \\ \delta b_z^N \cos(\theta) & \delta b_z^N \sin(\theta) & \frac{\bar{b}_x^N + i\bar{b}_y^N}{\sqrt{2}} & \frac{\bar{b}_x^N - i\bar{b}_y^N}{\sqrt{2}} & 0 \end{pmatrix}. \quad (34)$$

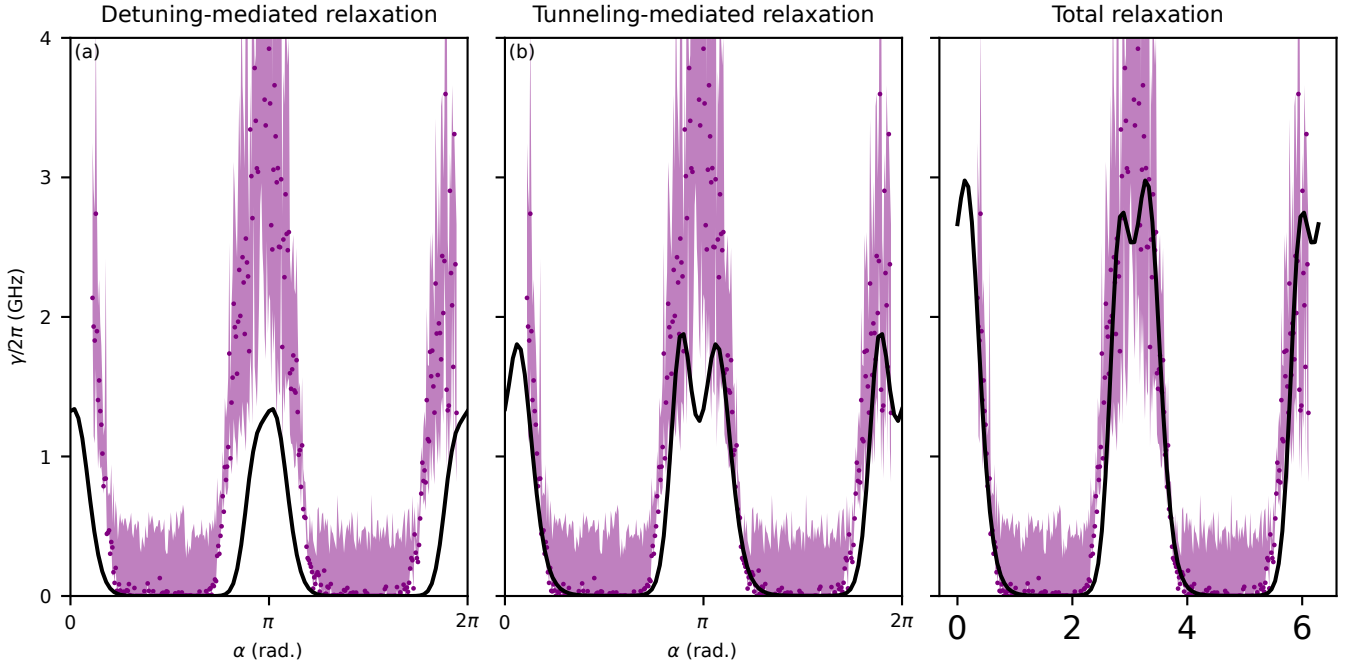


FIG. 2. **Phonon-mediated noise.** Both subfigures show the experimental data for the total dephasing rates (purple). (a) Black curve represents relaxation due to phonons-mediated tunnelling, $\gamma_1^{t_c}/2$ (b) Black curve represents relaxation due to phonons-mediated detuning, $\gamma_1^\varepsilon/2$. Both quantities are given by Eq. (28), where $i = t_c, \varepsilon$. (c) Total phonon-mediated relaxation $\gamma_1^{\text{ph}}/2 = \gamma_1^{t_c}/2 + \gamma_1^\varepsilon/2$

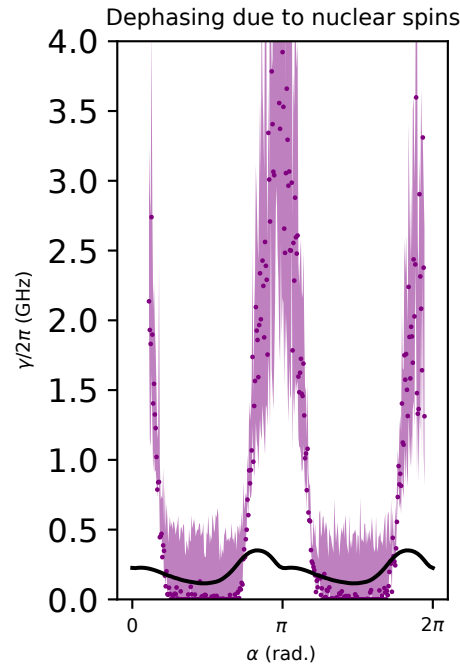


FIG. 3. **Hyperfine interaction-mediated noise.** Dephasing noise due to magnetic noise from the nuclear spin bath. The solid curve is given by $\sqrt{\langle \delta_z^N \delta_z^N \rangle} / \sqrt{2\hbar}$. For plotting the black curve, we use a larger value of $1/\tau$ than expected to magnify the trend of the nuclear-spin induced noise.

Here the quantization axes are aligned to the total Zeeman energy, but we omit the index ' to simplify the notation.

To model the nuclear spins, we assume that the magnetic fields in the two dots differ by a random amount, thus leading to decoherence. The dynamics of the nuclear spins is typically slow and has low amplitude at large frequencies, and we restrict ourselves to the description of the dephasing rates and model the nuclear spin as sources of quasi-static noise, with spectral function $S_{\varphi\varphi} = \pi\delta(\omega)\hbar^2\Gamma_N^2$. This noise produces the typical Gaussian decay $e^{-\Gamma_N^2 t^2}$, rather than exponential.

To evaluate the rate $\Gamma_N = \sqrt{\langle\delta_z^N\delta_z^N\rangle}/\sqrt{2}\hbar$, we follow the same procedure used above and we project H_M onto the lowest spin states in order to find the noise Hamiltonian H_N^D in Eq. (2). We then assume uncorrelated and isotropic noise identical in amplitude in both dots, i.e. $\mu_B^2\langle(\delta\mathbf{B}_N^i)_n(\delta\mathbf{B}_N^j)_m\rangle = \delta_{ij}\delta_{mn}\hbar^2/\bar{\tau}^2$, such that

$$\mu_B^2\langle(\delta b_N)_n(\delta b_N)_m\rangle = \mu_B^2\langle(\bar{b}_N)_n(\bar{b}_N)_m\rangle = \frac{\hbar^2}{4\bar{\tau}^2}(B_{nm}^L + B_{nm}^R) , \quad (35)$$

$$\mu_B^2\langle(\delta b_N)_n(\bar{b}_N)_m\rangle = \frac{\hbar^2}{4\bar{\tau}^2}(B_{nm}^L - B_{nm}^R) , \quad (36)$$

$$\underline{B}^{L,R} = \underline{R}^T(\mp\theta_{\text{so}}/2)\underline{g}_{L,R}^T\underline{g}_{L,R}\underline{R}(\mp\theta_{\text{so}}/2) . \quad (37)$$

We overlay the results of the numerical calculation on the data in Figure 3 and note that it does not capture the order-of-magnitude dependence on the B -field alignment. Interestingly, we observe a similar anti-correlation with respect to the coupling to resonator, although with a much smaller amplitude of oscillation compared to the experimentally measured one. This gives us confidence that the compromise-free sweet spot makes the qubit more resilient against also against nuclear spin noise.

An alternative way to find an upper limit of the nuclear spin-induce decoherence is to consider the characteristic rate $\bar{\tau}$. We estimate the expected value as $\bar{\tau}^{-1} \approx \sqrt{\sum_k \nu_k I_k (I_k + 1) A_k^2 / \hbar^2 N}$, where $N \sim 10^8$ is the number of atoms in the dot and ν_k the percentage of spinful nuclei k with spin I_k and hyperfine coupling $A_k \sim 300 \text{ }\mu\text{eV}$. We then find that $\Gamma_N \propto 1/\bar{\tau} \sim 0.1 \text{ GHz}$ which is much lower than the measured decoherence for fields perpendicular to the nanowire.

IV. CONCLUSION

The calculations of the decoherence for various decoherence sources allow to exclude most of them as dominant in our experiments. By matching the trend expected by theoretical estimation with our measurement, we conclude that only magnetic noise stemming from nuclear spins and phonons are consistent with the experimental data.

[1] V. N. Golovach, A. Khaetskii, and D. Loss, *Physical review letters* **93**, 016601 (2004).
[2] V. Kornich, C. Kloeffel, and D. Loss, *Quantum* **2**, 70 (2018).
[3] L. Cywiński, R. M. Lutchyn, C. P. Nave, and S. D. Sarma, *Physical Review B* **77**, 174509 (2008).
[4] J. Zou, S. Bosco, and D. Loss, *npj Quantum Information* **10**, 46 (2024).
[5] C. Kloeffel, M. Trif, and D. Loss, *Physical Review B* **90**, 115419 (2014).
[6] M. Trif, V. N. Golovach, and D. Loss, *Physical Review B* **77**, 045434 (2008).